Layer degree of freedom for excitons in transition metal dichalcogenides

Sarthak Das, Garima Gupta, and Kausik Majumdar[*]

Department of Electrical Communication Engineering, Indian Institute of Science, Bangalore 560012, India

Layered transition metal dichalcogenides (TMDCs) host a variety of strongly bound exciton complexes that control the optical properties in these materials. Apart from spin and valley, layer index provides an additional degree of freedom in a few-layer-thick film. Here we show that in a few-layer TMDC film, the wave functions of the conduction and valence-band-edge states contributing to the K (K') valley are spatially confined in the alternate layers—-giving rise to direct (quasi-)intralayer bright exciton and lower-energy interlayer dark excitons. Depending on the spin and valley configuration, the bright-exciton state is further found to be a coherent superposition of two layer-induced states, one (E type) distributed in the even layers and the other (O type) in the odd layers. The intralayer nature of the bright exciton manifests as a relatively weak dependence of the exciton binding energy on the thickness of the few-layer film, and the binding energy is maintained up to 50 meV in the bulk limit—-which is an order of magnitude higher than conventional semiconductors. Fast Stokes energy transfer from the intralayer bright state to the interlayer dark states provides a clear signature in the layer-dependent broadening of the photoluminescence peak, and plays a key role in the suppression of the photoluminescence intensity observed in TMDCs with thickness beyond a monolayer.

I. INTRODUCTION

The binding energy of an exciton is a strong function of quantum confinement of the electrons and holes. A two-dimensional exciton is thus expected to exhibit stronger binding energy than its three-dimensional counterpart [1]. This, coupled with heavy carrier effective mass [2,3], and small dielectric constant [3–5], results in a large binding energy of excitons in monolayer transition metal dichalcogenide (TMDC) materials [4–9]. This has led to recent efforts in exploring the physics of various exciton complexes including excitons [10], biexcitons [11], trions, and their dark states [10,12,13], using monolayer TMDC as a test bed. The inversion symmetry of the crystal is broken in the monolayer limit, and more generally, in TMDCs with an odd number of layers, giving rise to rich spin and valley physics [7,14,15]. While exciton complexes have been extensively studied in monolayer TMDCs, the effort in few-layer-thick films remains limited [16–23]. This is primarily due to the transition from direct band gap in monolayer to indirect band gap in few layer, suggesting fast relaxation of valley carriers from the K (K') points. Also, inversion symmetry is either explicitly restored (in even number of layers) or smears out (in odd number of layers) in multilayer films, suppressing valley controllability.

On the other hand, few-layer films allow the provision to use layer as an additional degree of freedom. In the 2H structure of TMDCs, the consecutive layers are rotated by 180° with respect to each other [24]. Consequently, the electrons at the K point in a bilayer system are not allowed to spill over the other layer due to the symmetry of the constituent d_{z^2} orbital contributing to the conduction band. On the other hand, for the holes, there exists a finite interlayer coupling. However, there is also a large spin splitting in the valence band, the magnitude of which is larger than the interlayer coupling term. This results in a confinement of the holes to a single layer as well. The spilling of the hole wave function to the consecutive layers is particularly weak in W-based TMDCs [25,26] compared with Mo-based TMDCs owing to larger spin-orbit interaction. Such suppression of interlayer hopping for both electrons and holes in bilayer TMDCs gives rise to layer pseudospin [24].

However, this argument of single-layer confinement is strictly true only at the K (K') points of the Brillouin zone, particularly for few-layer-thick film with number of layers more than two. On the contrary, the momentum-space distribution of exciton, as predicted from the Bethe-Salpeter (BS) equation [27], spreads well beyond the K (K') points, and the wave functions spill over to the other layers due to band mixing. In this work, taking the finite momentum-space distribution of excitons into account, we generalize the concept of layer degree of freedom for an arbitrary number of layer thickness of WSe_2 in the context of the direct exciton to reveal three important properties. First, for a given spin and valley, the layer degree of freedom introduces an additional selection rule for optical brightness. This results from intra- and interlayer spatial distribution of excitons arising due to electron and hole wave functions being distributed either in the odd or in the even layers. Second, the nonradiative scattering from the bright intralayer to the dark interlayer states has a clear signature in the layer-dependent luminescence linewidth, and plays a key role in luminescence suppression in few-layer TMDC. Third, owing to a pseudoconfinement arising from the quasi-intralayer nature of the bright exciton, its binding energy is a relatively weak function of thickness of the film, and

*kausikm@iisc.ac.in
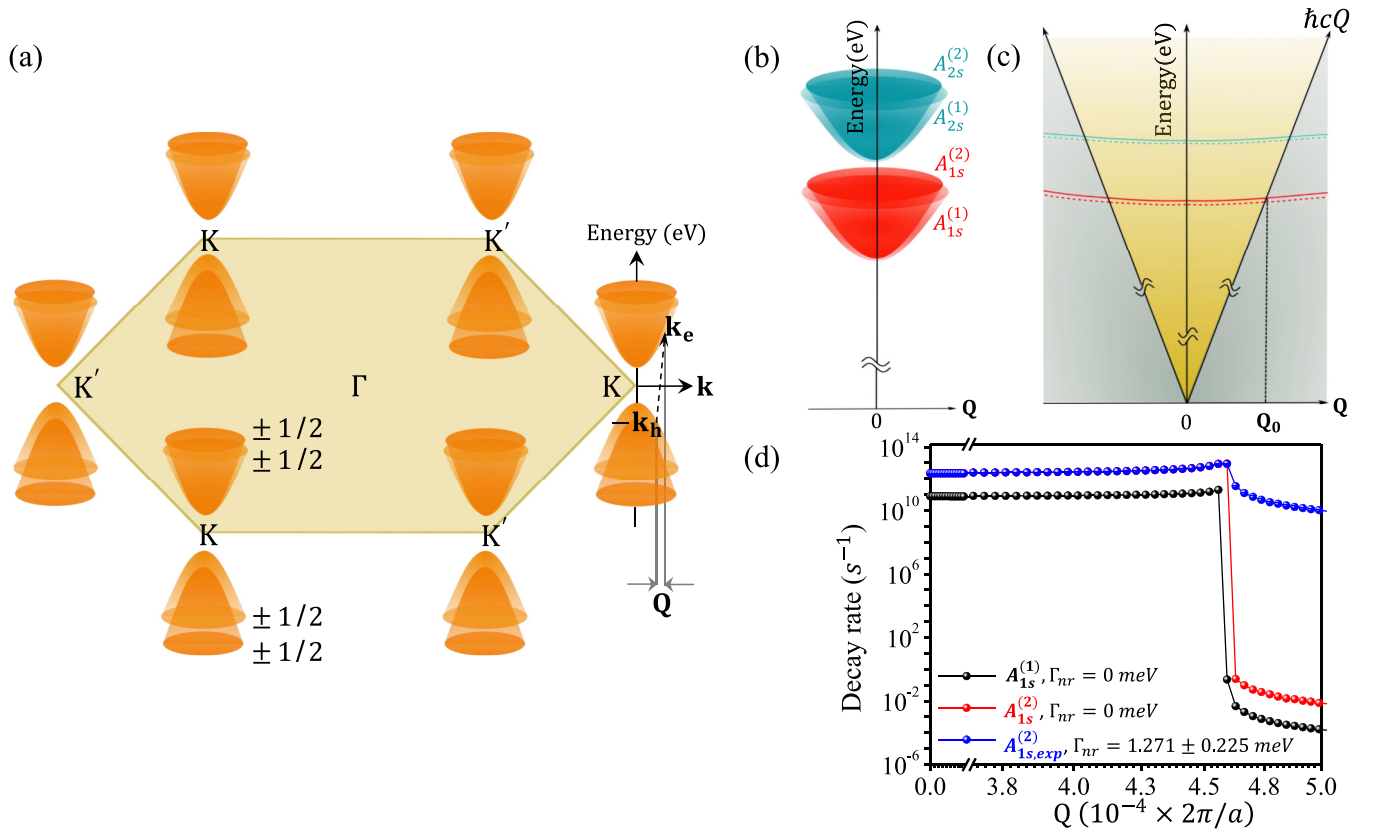
FIG. 1. Electronic and excitonic band structure in bilayer TMDCs. (a) Band diagram showing the conduction band (CB) and valence band (VB) around the corners of the hexagonal Brillouin zone in bilayer TMDCs. Each band is spin degenerate. (b) Exciton band dispersion of $1s$ and $2s$ excitons with its center-of-mass momentum ($\mathbf{Q}$). Contrary to a monolayer system, there are two possible $1s$ states arising from layer degree of freedom. (c) Light cone for excitons, where $\mathbf{Q}_0$ is the edge of the conventional light cone, and the boundary of the light cone is given by the light line $\hbar cQ$. The excitons occupying the lower-energy $A_{1s}^{(1)}$ and $A_{2s}^{(1)}$ bands (dashed line) are dark in nature because of their interlayer character, whereas the higher-energy $A_{1s}^{(2)}$ and $A_{2s}^{(2)}$ excitons (solid line) are bright due to their intralayer character. (d) Radiative decay rate variation of the two $1s$ exciton bands in (b) with $\mathbf{Q}$ (in units of $10^{-4}\frac{2\pi}{a}$) on varying the nonradiative linewidth of the exciton band. In the absence of nonradiative scattering ($\Gamma_{NR} = 0$), the decay rate of the $A_{1s}^{(2)}$ exciton (red) is roughly two orders of magnitude larger than the $A_{1s}^{(1)}$ exciton (black), showing that the lower-energy $A_{1s}^{(1)}$ exciton is radiatively inefficient compared to the higher-energy $A_{1s}^{(2)}$ state. As Γ_{NR} increases, the decay rate outside the light cone boundary $\mathbf{Q}_0$ for the bright $A_{1s}^{(2)}$ exciton increases due to enhanced participation of the broadened exciton states above the light line.

remains significantly large (~ 50 meV) even in the bulk limit [28–30] compared to conventional semiconductors [31,32].

II. EXCITON STATES IN FEW-LAYER TMDC AND THEIR RADIATIVE DECAY

To understand the excitonic structure in a few-layer TMDC, we model the exciton using a combination of $\mathbf{k} \cdot \mathbf{p}$ Hamiltonian and Bethe-Salpeter theory [27,33]. Each layer of WSe$_2$ belongs to the C_{3h} point group at the high-symmetry K and K' points of the Brillouin zone, and the W atoms have a trigonal prismatic coordination with the Se atoms. Close to the band edges around the K and K' points in the Brillouin zone [(Fig. 1(a)], the bands are contributed primarily from the W d orbitals. The symmetry-driven basis states for the conduction- and the valence-band edges for the lth layer can be written as [26] $|c\rangle = |5d_{z^2}^l\rangle$ and $|v\rangle = \frac{1}{\sqrt{2}}(|5d_{x^2-y^2}^l\rangle + i\tau_z|5d_{xy}^l\rangle)$, respectively. Here $\tau_z = \pm 1$ are the K and K' valley indices. For AB stacked TMDC, the adjacent layers are rotated by $180°$ around the c axis. The Hamiltonian for an n-layer WSe$_2$ film

is obtained by expanding the monolayer $\mathbf{k} \cdot \mathbf{p}$ Hamiltonian upon incorporating the interlayer coupling of the VBs with the immediate neighbor layers [24]. In Supplemental Material S1 [34], we show the generalized multilayer Hamiltonian used in this work. In the same Supplemental Material [34], we also show the Hamiltonians for the bilayer (2L), trilayer (3L), and four-layer (4L) systems explicitly.

An exciton state $|\Psi_s(\mathbf{Q})\rangle$ in an exciton band s at a center-of-mass momentum $\mathbf{Q} = \mathbf{k}_e + \mathbf{k}_h$ is a coherent superposition of hole (with crystal momentum $\mathbf{k}_h$) and electron (with crystal momentum $\mathbf{k}_e$) states from band pairs (v, c) in an n-layer system in the reciprocal space and can be written as

$$|\Psi_s(\mathbf{Q})\rangle = \sum_{v,c,\mathbf{k}} \lambda_{v,c,\mathbf{Q}}^{(s)}(\mathbf{k})|v, \mathbf{k}\rangle|c, \mathbf{k}+\mathbf{Q}\rangle. \quad (1)$$

$\lambda_{v,c,\mathbf{Q}}^{(s)}(\mathbf{k})$ and the exciton eigen energies $E_{ex}^{(s)}(\mathbf{Q})$ are obtained from the solution of the BS equation [27]:

$$\langle v, c, \mathbf{k}, \mathbf{Q}|H|v', c', \mathbf{k}', \mathbf{Q}\rangle$$
$$= \delta_{vv'}\delta_{cc'}\delta_{\mathbf{kk}'}(\varepsilon_{(\mathbf{k}+\mathbf{Q})c} - \varepsilon_{\mathbf{k}v}) - (\xi - \varrho)_{vv'}^{cc'}(\mathbf{k}, \mathbf{k}', \mathbf{Q}). \quad (2)$$

Here ε is the quasiparticle energy eigenvalue obtained by diagonalizing the quasiparticle Hamiltonian in Supplemental Material S1 [34]. ϱ is the exchange term and we neglect this term since in this work as we are primarily interested in the exciton band structure for the direct exciton at K (K'), with $\mathbf{Q} \approx 0$. The direct term ξ is evaluated using the Keldysh form of the Coulomb interaction potential [27]: $V_q = \frac{2\pi e^2}{\kappa q (1 + r_0 q)}$. The effective dielectric constant κ and the characteristic screening length r_0 are used as fitting parameters which we vary with the number of layers in the TMDC film.

In the rest of the paper, we only consider the spin-allowed, bright transitions, and ignore the selection rule governed dark excitons. Also, we shall limit our discussions to A-series excitons only, keeping in mind there exist higher-energy exciton series (for example, B series and above). Figure 1(a) schematically illustrates the one-particle band structure for bilayer WSe$_2$. The low-energy bands (1s and 2s) of the A-series exciton in the $\mathbf{Q}$ space are shown in Fig. 1(b). In bilayer, for each of A_{1s} and A_{2s} excitons, there are two layer-induced exciton bands [for example, $A_{1s}^{(1)}$ and $A_{1s}^{(2)}$ for 1s states], which are closely spaced in energy.

Figure 1(c) shows the light cone, within which the energy- and momentum-conservation laws are obeyed during an exciton recombination to emit a photon. Thus, any spin-allowed bright-exciton state with Q < Q$_0$ can emit light by radiative recombination. Owing to the small momentum of the photon

compared to the in-plane momentum of the exciton, the light cone constitutes of a small part ($< 0.1\%$) of the Brillouin zone. To compare the strength of the photoluminescence from the different exciton states, we evaluate the radiative decay rate using the following relation [35,36]:

$$
\Gamma_R(\mathbf{Q}) = \eta_o \frac{\hbar e^2}{2 m_o^2}
$$

$$
\times |\chi_{\mathrm{ex}}(\mathbf{Q})|^2 \int_0^{\infty} dq_z \frac{1}{\sqrt{Q^2 + q_z^2}} \times \left(1 + \frac{q_z^2}{Q^2 + q_z^2} \right)
$$

$$
\times \frac{\Gamma(\mathbf{Q})/\pi}{\left[E_{\mathrm{ex}}(\mathbf{Q}) - \hbar c \sqrt{Q^2 + q_z^2} \right] + \Gamma(\mathbf{Q})^2} \cdots \quad (3)
$$

Here $\Gamma(\mathbf{Q})$ is the total radiative and nonradiative broadening: $\Gamma(\mathbf{Q}) = \Gamma_R(\mathbf{Q}) + \Gamma_{NR}$. We assume Γ_{NR} to be $\mathbf{Q}$ independent for simplicity. See Supplemental Material [34] for detailed calculation of $\chi_{\mathrm{ex}}(\mathbf{Q})$. Note that Eq. (3) is a self-consistent equation and provides the fundamental radiative broadening of the exciton states when $\Gamma_{NR} = 0$. Figure 1(d) shows the calculated intrinsic radiative decay rate (for $\Gamma_{NR} = 0$) for both $A_{1s}^{(1)}$ (in black) and $A_{1s}^{(2)}$ (in red) as a function of $\mathbf{Q}$ for bilayer WSe$_2$. The implications of the large difference between the two rates will be discussed later.
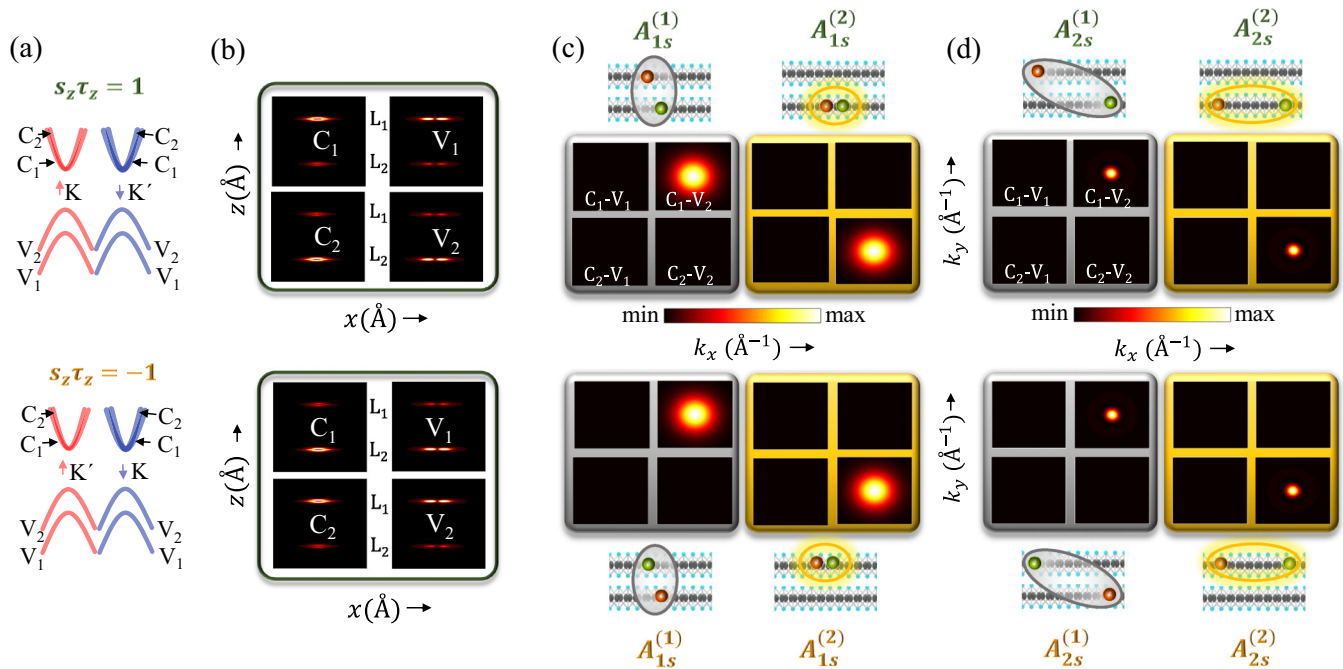
FIG. 2. Exciton formation in 2L WSe$_2$. (a) Schematic of layer-induced bands at the zone corner for different spin (s_z) and valley (τ_z) configurations. V$_i$ and C$_i$ correspond to the ith valence and conduction band, respectively. The spin and valley configuration for the top and bottom rows has been followed in the subsequent figures also. (b) Real-space distribution of different bands at $\boldsymbol{k} = \boldsymbol{K} + \Delta\boldsymbol{k}$, with $\Delta\boldsymbol{k} = \frac{2\pi}{a}(0.0033,\ 0.0033)$ with the same spin and valley configuration indicated in (a). CBs and VBs are shown in the left and right panels, respectively. The physical locations of the layers are shown in the middle. (c), (d) $\boldsymbol{k}$-space distribution of (c) the A_{1s} exciton and (d) the A_{2s} exciton, for all the possible individual transitions for a bilayer system. The two different A_{1s} states have been indicated according to their dark (in gray boxes) and bright (in yellow boxes) nature. The corresponding real-space layer-resolved distribution for each exciton configuration (green and copper spheres indicate the hole and the electron, respectively) is illustrated schematically above the top panel and below the bottom panels. A_{2s} excitons are more separated in real space while more confined in the k space.

III. LAYER DISTRIBUTION OF EXCITON STATES—LAYER-INDUCED BRIGHT AND DARK STATES

Figure 2(a) schematically shows the conduction and the valence bands of 2L WSe$_2$ for a given spin- (s_z) and valley (τ_z) index. The top panel describes the doubly degenerate case $\tau_z s_z = 1$, which includes ($\tau_z = 1$; $s_z = 1$) and ($\tau_z = -1$; $s_z = -1$), while the bottom panel describes the other doubly degenerate case $\tau_z s_z = -1$, including ($\tau_z = 1$; $s_z = -1$) and ($\tau_z = -1$; $s_z = 1$). At $k = K$, owing to the weak interlayer coupling, states from both conduction- and valence bands are confined to either layer L$_1$ or L$_2$, respectively. However, this is not strictly true for $k \neq K$. As an example, Fig. 2(b) shows the layer distribution of the band-edge electron and hole states in 2L WSe$_2$ for $k = K + \Delta k$, with $\Delta k = 2\pi/a(0.0033, 0.0033)$, where $a = 3.28$ Å.

The momentum- and transition-resolved probability distribution ($|\lambda_{v,c,\mathbf{Q}=0}^{(s)}(\mathbf{k})|^2$) of the lowest-lying [$A_{1s}^{(1)}$ and $A_{1s}^{(2)}$] and the next-higher-energy [$A_{2s}^{(1)}$ and $A_{2s}^{(2)}$] direct excitons, as obtained from the BS equation, is shown in Figs. 2(c) and 2(d). Note that each exciton predominantly consists of a single transition between a specific (v, c) band pair, with negligible contribution from the other transitions. The real-space layer distribution of the dominant transition for each exciton state is also schematically shown in Figs. 2(c) and 2(d). The unique layer distribution of the electron and hole basis states governs

the formation of intralayer and interlayer exciton. For example, for $\tau_z s_z = 1$, the lower-energy exciton [$A_{1s}^{(1)}$] almost entirely arises from C_1V_2 transition, and hence is an interlayer exciton as inferred from the top panel of Fig. 2(b). On the other hand, the higher-energy exciton [$A_{1s}^{(2)}$] results primarily from C_2V_2 transition and hence forms an intralayer exciton confined in the bottom layer. For $\tau_z s_z = -1$, the intralayer exciton is confined in the top layer, as explained in the bottom panel of Fig. 2(b). Also note that with an increase in quantum number (from 1s to 2s), the more confined areal distribution of the exciton in the k space suggests a larger spread in real-space distribution.

The intra- and interlayer spatial distributions of the different exciton states are expected to strongly affect their radiative decay. As mentioned earlier, since all these excitons are spin-allowed bright states, any exciton with **Q** lying within the light cone [in Fig. 1(c)] can, in principle, recombine radiatively emitting photons in a spontaneous fashion. However, in Fig. 1(d), we observe that $A_{1s}^{(1)}$ exciton is an order of magnitude weaker compared to the $A_{1s}^{(2)}$ state in terms of light emission due to its interlayer nature. The primary contributing orbitals (W 5d) for the excitons exhibit a spatial extent along the out-of-plane (z) direction that is much smaller than the interlayer separation [see Fig. 2(b)], suppressing the matrix element for the decay rate in the case of interlayer
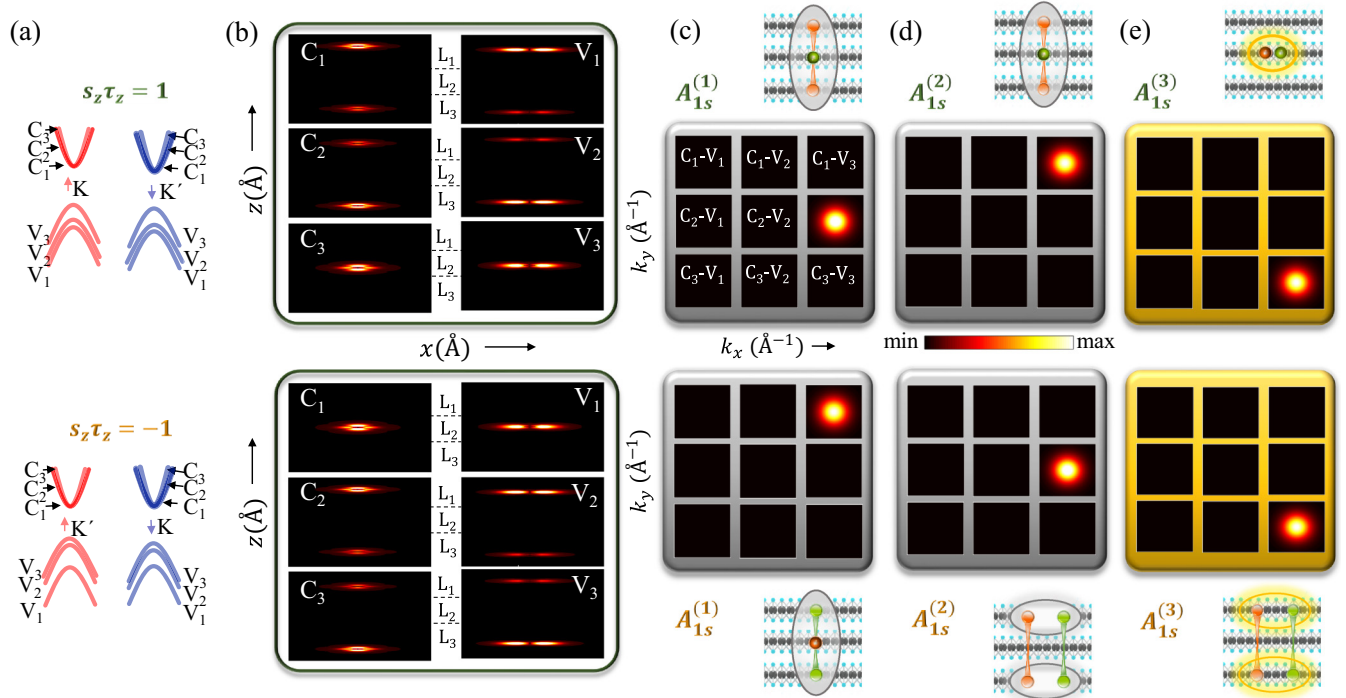
FIG. 3. Exciton formation in 3L WSe$_2$. (a) Schematic of layer-induced bands at the zone corner for different spin- (s_z) and valley (τ_z) configurations. V$_i$ and C$_i$ correspond to the ith valence and conduction band, respectively. (b) Real-space distribution of different bands at $k = K + \Delta k$, with $\Delta k = 2\pi/a(0.0033, 0.0033)$ with the same spin valley configuration indicated in (a). The conduction and valence bands are shown in the left and right panels, respectively. The physical locations of the layers are shown in the middle. (c)–(e) k-space distribution of the A_{1s} exciton for all the possible individual transitions for a trilayer system. The three different A_{1s} states have been indicated according to their dark (in gray boxes) in (c), (d) and bright (in yellow boxes) nature in (e). The corresponding real-space layer-resolved distribution for each exciton configuration (green and copper spheres indicate the hole and the electron, respectively) is illustrated schematically above the top panel and below the bottom panels. Depending on layer distribution, low-energy $A_{1s}^{(1)}$ and $A_{1s}^{(2)}$ forms the interlayer excitons in (c), (d) while the high-energy $A_{1s}^{(3)}$ forms the intralayer excitons in (e).

exciton. Henceforth, we call these interlayer states layer-induced dark excitons. We can thus conclude that the light emission from the $1s$ state predominantly happens due to the radiative recombination of the intralayer $A_{1s}^{(2)}$ exciton.

The analysis can be readily extended to the 3L system, and the results are summarized in Fig. 3, where three different layer-induced $1s$ excitons (from the A series) are formed, namely $A_{1s}^{(1)}$, $A_{1s}^{(2)}$, and $A_{1s}^{(3)}$. Figure 3(a) schematically shows the electronic band structure around K and K' points. Similar to bilayer, the components of the eigenstates are significant only in the alternate layers, that is, they are either confined to the even layers or to the odd layers, as illustrated in Fig. 3(b). The transition- and momentum-resolved probability distribution of the resulting A_{1s} excitons are explicitly shown in Figs. 3(c)–3(e). The probability distributions indicate the dominance of one transition out of nine possible transitions for an exciton. Similar to the bilayer case, the resulting excitons also follow interlayer pattern for low-energy [$A_{1s}^{(1)}$ and $A_{1s}^{(2)}$] excitons, while intralayer pattern for the higher-energy [$A_{1s}^{(3)}$] state. Interestingly, for $\tau_z s_z = 1$, the $A_{1s}^{(3)}$ exciton is confined in the middle layer (L_2), as shown in the top panel of Fig. 3(e). However, for the other spin-valley configuration ($\tau_z s_z = -1$), the $A_{1s}^{(3)}$ exciton is confined to the L_1 and L_3 [bottom panel of Fig. 3(e)]. Thus, it maintains its intralayer structure, but gets distributed in the odd-numbered layers. We term the latter case as quasi-intralayer exciton. The calculated

decay rates of the different exciton states for trilayer WSe$_2$ are shown in Supplemental Material S3 [34]. Both types of $A_{1s}^{(3)}$ excitons exhibit more than an order of magnitude higher decay rate compared to the rest, and are responsible for photoluminescence.

In Fig. 4, we schematically depict the real-space layer-resolved distribution of only the bright excitons ($A_{1s}^{(n)}$), for bilayer- to six-layer (6L)-thick WSe$_2$ films. We can generalize that for an n-layer-thick TMDC, there are two doubly degenerate bright (quasi)intralayer excitons. The rest of the $2n$-2 exciton states are interlayer and hence layer-induced dark in nature, which are otherwise bright from a conventional selection rule (spin and azimuthal quantum number selection) perspective. Between the two doubly degenerate bright excitons, one exciton is distributed in the even layers and the other in the odd layers, and we call them E-type (with layer index $l_z = +1$) and O-type ($l_z = -1$) exciton, respectively. In the case of 1L and 2L systems, the bright excitons are confined to a single layer. For 3L system, the E-type exciton is confined to a single (middle) layer, while the O-type one is quasi-intralayer in nature, being distributed between the top and the bottom layers. For 4L and thicker samples, we only have quasi-intralayer doubly degenerate E- and O-type bright excitons. A careful observation reveals that the spin, valley, and layer indices of a bright exciton are coupled by the simple rule $l_z s_z \tau_z = +1$, which dictates the possible quantum states allowed in a few-layer TMDC system.
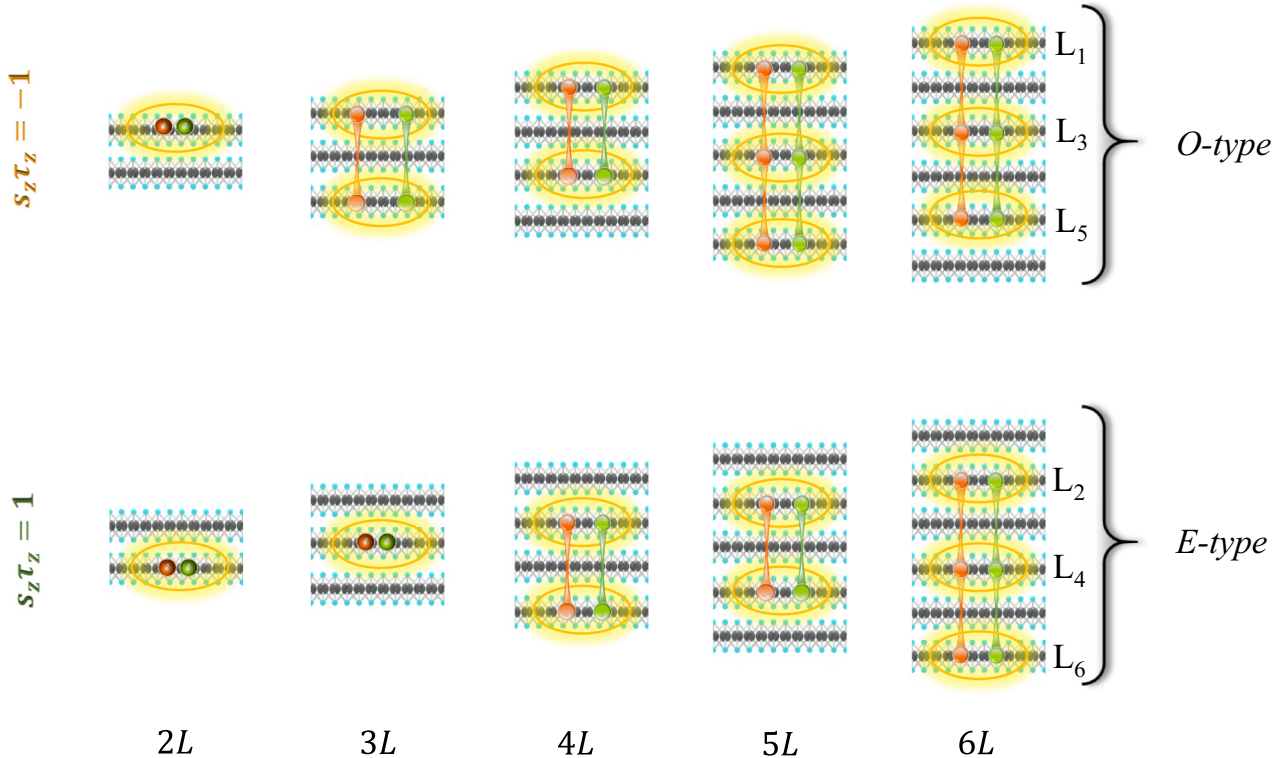
FIG. 4. Layer distribution of bright excitons. Schematic for the real-space layer-resolved distribution of different intralayer bright-exciton states for 2L to 6L for two doubly degenerate configurations. Depending on their layer distribution, these are classified as O-type (distributed in the odd-numbered layers, top panel, layer index $l_z = -1$) and E-type (distributed in the even-numbered layers, bottom panel, layer index $l_z = +1$) excitons.
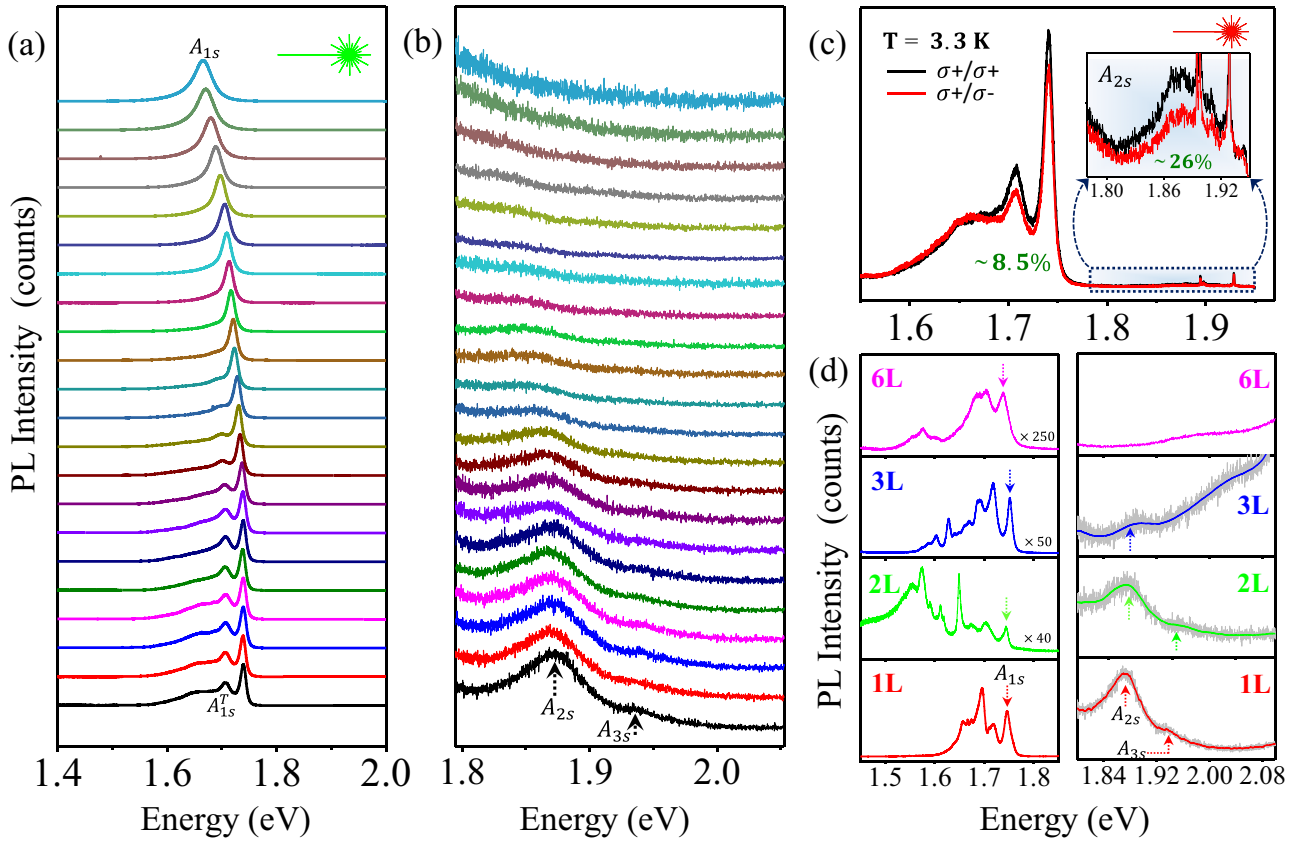
FIG. 5. Exciton states in WSe$_2$ probed through photoluminescence. (a) PL intensity variation of 1L WSe$_2$ at sample temperature ranging from 3.3 to 295 K with 532-nm laser excitation. Corresponding exciton (A_{1s}) and trion (A_{1s}^T) peaks are indicated. (b) Magnified view of the higher-order exciton (A_{2s} and A_{3s}) peaks with increasing temperature, as indicated by arrows. (c) Circular polarization-resolved PL spectra for monolayer WSe$_2$ with a 633-nm laser excitation at 3.3 K with a polarization contrast (ρ) of ~8.5% for A_{1s}. Inset: Degree of polarization of A_{2s} peak is around 26%. (d) PL spectra of 1L, 2L, 3L, and 6L WSe$_2$, with 532-nm laser excitation at 3.3 K in the left panel. PL spectra showing higher-order exciton peaks (A_{2s} and A_{3s}) for the same samples in (d) in the right panel. The higher-order peaks (indicated by arrows) are discernible only for 1L, 2L, and 3L samples.

IV. EXPERIMENTAL EVIDENCE AND IMPLICATIONS

We next explore indirect experimental evidences and subsequent implications of the above-mentioned layer distribution of the exciton states. In order to do so, we employ temperature-dependent photoluminescence measurement from WSe$_2$ films of varying layer thickness.

A. Experiment

We mechanically exfoliate WSe$_2$ flakes on a clean Si substrate covered with 285-nm-thick SiO$_2$. The thickness of the flake is identified by a combination of Raman and atomic force microscopy (AFM). Photoluminescence (PL) measurement is carried out by varying the sample temperature from 3.3 K to room temperature. The pressure of the sample chamber is kept below 10^{-4} Torr at all measurement temperatures. The PL is collected through a $50\times$ objective with a numerical aperture of 0.5 in confocal mode. The optical power density on the sample is kept below 100 μW to avoid any laser-induced heating effect.

Figure 5 summarizes the temperature and thickness dependence of the acquired photoluminescence spectra from WSe$_2$ samples using a 532-nm laser excitation. In Fig. 5(a), both

the neutral (A_{1s}) and charged (A_{1s}^T) A-series exciton peaks are distinctly visible in the temperature range up to ~90 K for monolayer sample. The redshift of the peak positions with an increase in temperature is due to a corresponding decrease in the quasiparticle band gap. The weak but distinct 2s (A_{2s}) and 3s (A_{3s}) peaks of the A exciton are observed in the zoomed-in Fig. 5(b) around 1.87 and 1.93 eV, respectively, at $T = 3.3$ K, which smear out as the sample temperature is increased. To confirm that the higher-energy peaks originate from the higher-order free-exciton bright states, we perform polarization-resolved photoluminescence measurement at $T = 3.3$ K. The sample is excited with a σ^+ circularly polarized light from a 633-nm laser, and the emitted light is passed through a σ^+ or σ^- analyzer. The results for the 1L flake are summarized in Fig. 5(c). We observe that the A_{1s} exciton peak and the A_{1s}^T trion peak show a degree of circular polarization (ρ) of ~8.5 and ~10.2%, respectively, where $\rho = \frac{I_{\sigma^+} - I_{\sigma^-}}{I_{\sigma^+} + I_{\sigma^-}}$. In the inset of Fig. 5(c), we show a magnified portion of the next higher order peak, which shows a strong polarization contrast of ~26%, confirming its A_{2s} assignment. The enhancement of ρ from 1s to 2s is because the 633-nm laser excites the 2s excitons in a near-resonant manner, suppressing the depolarization due to intervalley scattering.
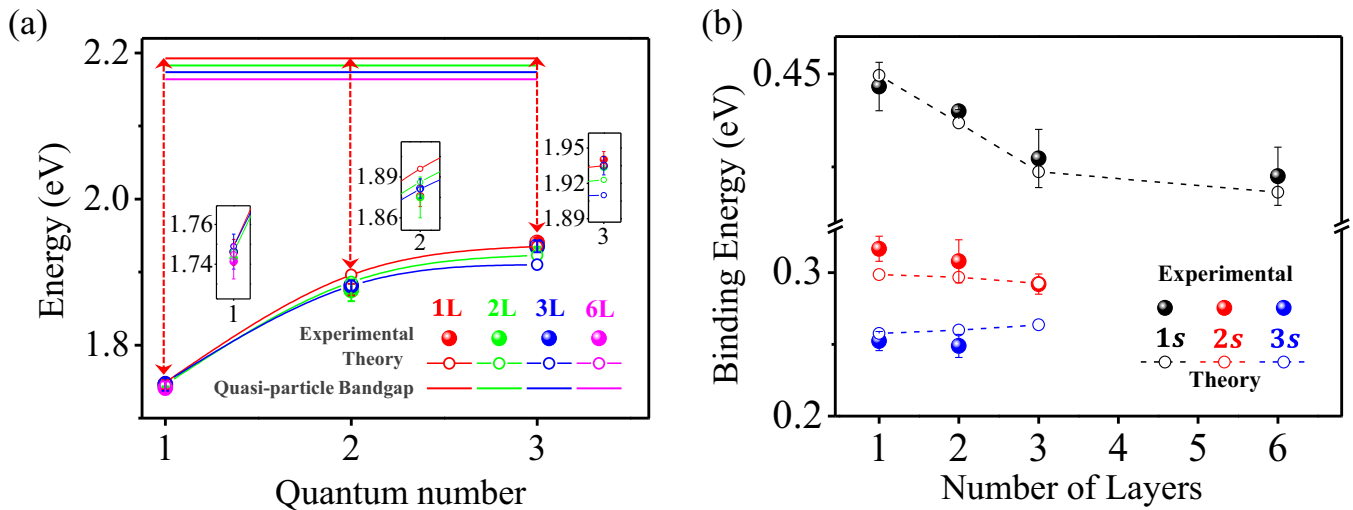
FIG. 6. Thickness-dependent binding energy of excitons. (a) PL emission energy plotted as a function of quantum number. The solid and open symbols represent the emission energies as obtained from photoluminescence experiment ("Experimental") and the Bethe-Salpeter equation ("Theory"), respectively. The Theory values correspond to the bright (quasi-)intralayer $A_{1s}^{(n)}$ exciton for the n-layer-thick film. The continuum, as obtained from the BS equation for different layers, is also shown as solid horizontal lines. The binding energy for a given state ($1s$, $2s$, $3s$) and sample thickness is extracted by subtracting the emission energy of that state from the corresponding continuum level, as indicated by the dashed red arrows for the 1L case. The zoomed-in view of the energy states corresponding to the individual quantum numbers are also shown in the insets. (b) The extracted binding energies from (a), plotted as a function of number of layers. Solid symbols represent experimental values, and open symbols with dashed lines indicate BS equation predicted (Theory) values.

In Fig. 5(d), we show the acquired PL spectra of WSe_2 flakes with varying thickness, namely 1L, 2L, 3L, and 6L, all taken at $T = 3.3$ K. In the left panel, apart from the neutral and charged exciton peaks, we also observe several peaks at energy lower than trion emission energy. The origin of these lower-energy peaks has been previously attributed to defect-bound localized excitons [10–12] and multiparticle excitonic states [10–13]. On the other hand, the higher-energy peaks, as shown in a magnified energy range in the right panel in Fig. 5(d), are only distinctly visible for 1L, 2L, and 3L cases.

B. Weak dependence of exciton binding energy on thickness

The positions of the A_{1s}, A_{2s}, and A_{3s} peaks remain almost unaltered (within ~5-meV error bar due to the variation in the individual spectrum obtained from these samples) irrespective of the thickness of the sample. Such layer independence of the A_{1s}-exciton peak position has been widely reported previously [37–40].

The (quasi-)intralayer nature of the bright exciton irrespective of the number of layers in the film forces a spatial pseudoconfinement of the exciton to individual layers. This allows the excitons to retain their two-dimensional character even in multilayer samples. This effect manifests itself as a weak dependence of the bright-exciton binding energy on the number of layers of the film. The bright excitons being accessible by photoluminescence experiment allows us to readily verify this hypothesis. The exciton emission energies, calculated from Eq. (2) for different layers, are plotted as a function of the quantum numbers in Fig. 6(a) as the open symbols, which are in good agreement with the experimental data, shown by the solid symbols. The insets show zoomed-in views of the data

from individual layers. The corresponding continuum levels obtained from the BS equation for different layer numbers are also shown in the same figure by solid horizontal lines. The corresponding binding energy of the different exciton states is then calculated by taking the difference between the continuum level and the emission energy (obtained from both photoluminescence spectra as well as BS equation) and plotted as a function of the thickness of the WSe_2 flake in Fig. 6(b). The agreement between BS theory and experiment is quite remarkable. The observation of the weak dependence of the exciton binding energy on WSe_2 film thickness is in stark contrast with a conventional semiconductor when the out-of-plane quantum confinement is relaxed. Also, the binding energy of the exciton for bulk TMDC is about 50 meV, which was measured long ago [28–30]. This is about an order of magnitude higher than typical exciton binding energies of III–V semiconductor samples [31,32]. The retention of the large binding energy in the bulk limit is another implication of such quasi-intralayer configuration of the bright excitons in TMDCs, which maintains a quasi-two-dimensional nature due to layer confinement even in thick samples. A summary of the layer dependence on the energy and the binding energy of different excitonic states is provided in Supplemental Material S4 [34].

C. Layer-dependent exciton linewidth broadening

Using a Voigt fit to the exciton peaks for samples with varying layer thickness, we deconvolute the homogeneous (Lorentzian) and the inhomogeneous (Gaussian, shown in Supplemental Materials S5 [34]) components of the exciton photoluminescence linewidth. The extracted homogeneous
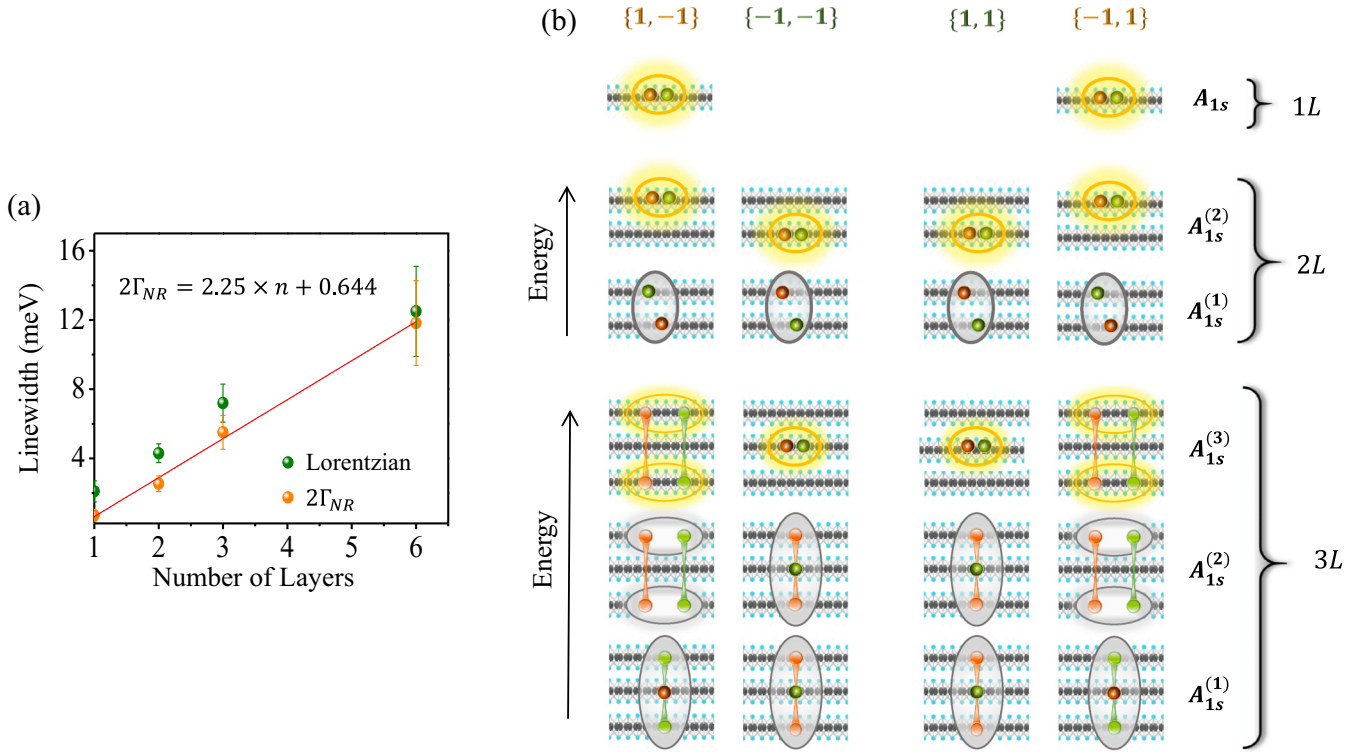
FIG. 7. Exciton scattering to interlayer dark states. (a) Experimental Lorentzian linewidth (green symbols) and the corresponding extracted nonradiative broadening $2\Gamma_{NR}$ (orange symbols), as a function of number of layers (n). Red line is the fitted function demonstrating linear relationship between nonradiative broadening and n. The fitted expression is shown in the inset. (b) Real-space layer-resolved distribution of the A_{1s} exciton for each spin-valley $\{s_z, \tau_z\}$ configuration for a monolayer (top panel), bilayer (middle panel), and a trilayer (bottom panel) system.

linewidth is found to increase monotonically as a function of number of layers (n) in Fig. 7(a) (green symbols). The total homogeneous linewidth is a result of both radiative and nonradiative dephasing processes. Using the self-consistency of Eq. (3), we deconvolute the corresponding nonradiative part $[2\Gamma_{NR}(n)]$ of the homogeneous broadening as a function of n from the photoluminescence homogeneous linewidth [36]. $2\Gamma_{NR}(n)$ (shown in orange symbols) is found to increase linearly with n. As the excitation density was maintained low ($<10^9$ cm^{-2}) during measurements, the exciton-exciton scattering-induced dephasing [41] is small, and the exciton-phonon scattering is the dominating nonradiative dephasing process in a monolayer sample in our experiment. For $n \geqslant 2$, apart from the exciton-phonon scattering within the bright $A_{1s}^{(n)}$ band, scattering to the indirect valleys (Γ and Λ) and to the lower-energy interlayer dark states are the additional nonradiative dephasing mechanisms. We assume that the phonon scattering within the $A_{1s}^{(n)}$ band is independent of layer number, and therefore is equal to the monolayer nonradiative linewidth (Γ_0). The layer dependence of the nonradiative linewidth can then be given by

$$\Gamma_{NR}(n) = \Gamma_0 + \Gamma_I + \sum_{i=1}^{n-1} \Gamma_{A_{1s}^{(n)} \to A_{1s}^{(i)}}; \quad n > 1 \quad (4)$$

Here, Γ_I quantifies the lumped effect of dephasing due to exciton-phonon scattering to the indirect valleys. Due to large intervalley momentum mismatch, Γ_I is expected to be

small compared to intravalley scattering rates. In the last term, $\Gamma_{A_{1s}^{(n)} \to A_{1s}^{(i)}}$ is the scattering of the bright (quasi-)intralayer $A_{1s}^{(n)}$ exciton to the ith dark interlayer $A_{1s}^{(i)}$ exciton, maintaining both their spin and valley indices (that is, conserving total angular momentum). Note that $A_{1s}^{(i)}$ ranges from $A_{1s}^{(1)} \to A_{1s}^{(n-1)}$, and this results in a proportionately increasing number of scattering channels as the number of layers increases [see Fig. 7(b) for 2L and 3L cases]. For a first-order estimate, we assume the same scattering rate [denoted by $\Gamma_{A_{1s}^{(B)} \to A_{1s}^{(D)}}$] from bright $A_{1s}^{(n)}$ to any of the ith lower-energy interlayer dark state. We can then rewrite Eq. (4) as

$$\Gamma_{NR}(n) = \Gamma_0 + \Gamma_I + (n-1)\Gamma_{A_{1s}^{(B)} \to A_{1s}^{(D)}}; \quad n > 1 \quad (5)$$

This explains the linear increment in the nonradiative exciton linewidth as the number of layers increases.

D. Photoluminescence suppression beyond monolayer

$\Gamma_{A_{1s}^{(B)} \to A_{1s}^{(D)}}$ is extracted from the slope of the linear fit from Fig. 7(a), and is found to be ~2.25 meV, which translates to a scattering rate of 3.4×10^{12} s^{-1} per channel. This is on the order of radiative decay rate of the bright exciton [see Fig. 1(d)] as well as the carrier transfer to indirect valleys [42]. Equation (5) suggests that with an increase in the number of layers, the total nonradiative decay rate due to intralayer to interlayer Stokes energy transfer increases proportionately. Since the interlayer states do not contribute to the luminescence, such

nonradiative scattering competes with the exciton radiative decay process. This suggests that apart from carrier transfer to the indirect valleys, the fast scattering to the interlayer dark states also plays a key role in suppressing luminescence in few-layer TMDCs.

V. CONCLUSIONS

In summary, the symmetry-driven even- and odd-layer distribution of the band-edge states close to the zone corner forces intra- (or quasi-intra-) and interlayer distribution of excitons in few-layer TMDCs. The intralayer exciton states exhibit more than an order of magnitude higher radiative decay rate compared to the interlayer states, and hence only these excitons contribute to the luminescence. These bright intralayer excitons can further be classified into E- and O-type excitons (denoted as layer index), depending on their spatial layer distribution over either even- or odd-numbered layers, respectively. This layer index (l_z) is coupled to the spin- (s_z) and valley (τ_z) indices by the rule $l_z s_z \tau_z = +1$. Such unique layer distribution has direct implication in maintaining large exciton binding energy in TMDCs up to the bulk limit. Further, the layer index (E or O) can be treated as an additional degree of freedom of the exciton quantum state in a few-layer system, and can be used for quantum information manipulation.

[1] X. L. Yang, S. H. Guo, F. T. Chan, K. W. Wong, and W. Y. Ching, Analytic solution of a two-dimensional hydrogen atom. I. Nonrelativistic theory, Phys. Rev. A **43**, 1186 (1991).

[2] K. Majumdar, C. Hobbs, and P. D. Kirsch, Benchmarking transition metal dichalcogenide MOSFET in the ultimate physical scaling limit, IEEE Electron Device Lett. **35**, 402 (2014).

[3] A. Ramasubramaniam, Large excitonic effects in monolayers of molybdenum and tungsten dichalcogenides, Phys. Rev. B **86**, 115409 (2012).

[4] K. He, N. Kumar, L. Zhao, Z. Wang, K. F. Mak, H. Zhao, and J. Shan, Tightly Bound Excitons in Monolayer WSe$_2$, Phys. Rev. Lett. **113**, 026803 (2014).

[5] H. P. Komsa and A. V. Krasheninnikov,Effects of confinement and environment on the electronic structure and exciton binding energy of MoS$_2$ from first principles, Phys. Rev. B **86**, 241201(R) (2012).

[6] A. Chernikov, T. C. Berkelbach, H. M. Hill, A. Rigosi, Y. Li, O. B. Aslan, D. R. Reichman, M. S. Hybertsen, and T. F. Heinz, Exciton Binding Energy and Nonhydrogenic Rydberg Series in Monolayer WS$_2$, Phys. Rev. Lett. **113**, 076802 (2014).

[7] X. Xu, W. Yao, D. Xiao, and T. F. Heinz, Spin and pseudospins in layered transition metal dichalcogenides, Nat. Phys. **10**, 343 (2014).

[8] H. Shi, H. Pan, Y. W. Zhang, and B. I. Yakobson, Quasiparticle band structures and optical properties of strained monolayer MoS$_2$ and WS$_2$, Phys. Rev. B **87**, 155304 (2013).

[9] G. Gupta, S. Kallatt, and K. Majumdar, Direct observation of giant binding energy modulation of exciton complexes in monolayer MoSe$_2$, Phys. Rev. B **96**, 081403 (2017).

[10] A. M. Jones, H. Yu, N. J. Ghimire, S. Wu, G. Aivazian, J. S. Ross, B. Zhao, J. Yan, D. G. Mandrus, D. Xiao *et al.*, Optical generation of excitonic valley coherence in monolayer WSe$_2$, Nat. Nanotechnol. **8**, 634 (2013).

[11] Y. You, X.-X. Zhang, T. C. Berkelbach, M. S. Hybertsen, D. R. Reichman, and T. F. Heinz, Observation of biexcitons in monolayer WSe$_2$, Nat. Phys. **11**, 477 (2015).

[12] X.-X. Zhang, T. Cao, Z. Lu, Y.-C. Lin, F. Zhang, Y. Wang, Z. Li, J. C. Hone, J. A. Robinson, D. Smirnov *et al.*, Magnetic brightening and control of dark excitons in monolayer WSe$_2$, Nat. Nanotechnol. **12**, 883 (2017).

[13] G. Wang, L. Bouet, D. Lagarde, M. Vidal, A. Balocchi, T. Amand, X. Marie, and B. Urbaszek, Valley dynamics probed through charged and neutral exciton emission in monolayer WSe$_2$, Phys. Rev. B **90**, 075413 (2014).

[14] W. Yao, D. Xiao, and Q. Niu, Valley-dependent optoelectronics from inversion symmetry breaking. Phys. Rev. B **77**, 235406 (2008).

[15] A. Srivastava, M. Sidler, A. V. Allain, D. S. Lembke, A. Kis, and A. Imamoğlu, Valley Zeeman effect in elementary optical excitations of a monolayer WSe$_2$, Nature Phys. **11**, 141 (2015).

[16] X. Dai, W. Li, T. Wang, X. Wang, and C. Zhai, Bandstructure modulation of two-dimensional WSe$_2$ by electric field, J. Appl. Phys. **117**, 084310 (2015).

[17] D. Li, R. Cheng, H. Zhou, C. Wang, A. Yin, Y. Chen, N. O. Weiss, Y. Huang, and X. Duan, Electric-field-induced strong enhancement of electroluminescence in multilayer molybdenum disulfide, Nat. Commun. **6**, 7509 (2015).

[18] M. Palummo, M. Bernardi,and J. C. Grossman, Exciton radiative lifetimes in two-dimensional transition metal dichalcogenides, Nano Lett. **15**, 2794 (2015).

[19] Y. Zhang, T.-R. Chang, B. Zhou, Y.-T. Cui, H. Yan, Z. Liu, F. Schmitt, J. Lee, R. Moore, Y. Chen *et al.*, Direct observation of the transition from indirect to direct bandgap in atomically thin epitaxial MoSe$_2$, Nat. Nanotechnol. **9**, 111 (2014).

[20] T. Brumme, M. Calandra, and F. Mauri, First-principles theory of field-effect doping in transition-metal dichalcogenides: Structural properties, electronic structure, Hall coefficient, and electrical conductivity, Phys. Rev. B **91**, 155436 (2015).

[21] X. Li, F. Zhang, and Q. Niu, Unconventional Quantum Hall Effect and Tunable Spin Hall Effect in Dirac Materials: Application to an Isolated MoS$_2$ trilayer, Phys. Rev. Lett. **110**, 066803 (2013).

[22] R. Roldán, M. P. López-Sancho, F. Guinea, E. Cappelluti, J. A. Silva-Guillén, and P. Ordejón, Momentum dependence of spin–orbit interaction effects in single-layer and multi-layer transition metal dichalcogenides, 2D Mater. **1**, 034003 (2014).

[23] R. Roldán, J. A. Silva-Guillén, M. P. López-Sancho, F. Guinea, E. Cappelluti, and P. Ordejón, Electronic properties of single-layer and multilayer transition metal dichalcogenides MX2 (M = Mo, W and X = S, Se), Ann. Phys. **526**, 347 (2014).

[24] Z. Gong, G.-B. Liu, H. Yu, D. Xiao, X. Cui, X. Xu, and W. Yao, Magnetoelectric effects and valley-controlled spin quantum gates in transition metal dichalcogenide bilayers, Nat. Commun. **4**, 2053 (2013).

[25] D. W. Latzke, W. Zhang, A. Suslu, T. R. Chang, H. Lin, H. T. Jeng, S. Tongay, J. Wu, A. Bansil, and A. Lanzara, Electronic structure, spin-orbit coupling, and interlayer interaction in bulk MoS2 and WS2, Phys. Rev. B **91**, 235202 (2015).

[26] D. Xiao, G.-B. Liu, W. Feng, X. Xu, and W. Yao, Coupled Spin and Valley Physics in Monolayers of MoS_2 and Other Group-VI Dichalcogenides, Phys. Rev. Lett. **108**, 196802 (2012).

[27] F. Wu, F. Qu, and A. H. Macdonald, Exciton band structure of monolayer MoS_2, Phys. Rev. B **91**, 075310 (2015).

[28] A. R. Beal, J. C. Knights, and W. Y. Liang, Transmission spectra of some transition metal dichalcogenides: II. group VIA: Trigonal prismatic coordination, J. Phys. C: Solid State Phys. **5**, 3540 (1972).

[29] A. R. Beal and W. Y. Liang, Excitons in 2H- WSe_2 and 3R-WS_2, J. Phys. C: Solid State Phys. **9**, 2459 (1976).

[30] J. A. Wilson and A. D. Yoffe, The transition metal dichalcogenides discussion and interpretation of the observed optical, electrical and structural properties, Adv. Phys. **18**, 193 (1969).

[31] R. L. Greene, K. K. Bajaj, and D. E. Phelps, Energy levels of Wannier excitons in $GaAs - Ga_{1-x}Al_x As$ quantum-well structures, Phys. Rev. B **29**, 1807 (1984).

[32] R. C. Miller, D. A. Kleinman, W. T. Tsang, and A. C. Gossard, Observation of the excited level of excitons in GaAs quantum wells, Phys. Rev. B **24**, 1134 (1981).

[33] D. Y. Qiu, T. Cao, and S. G. Louie, Nonanalyticity, Valley Quantum Phases, and Lightlike Exciton Dispersion in Monolayer Transition Metal Dichalcogenides: Theory and First-Principles Calculations, Phys. Rev. Lett. **115**, 176801 (2015).

[34] See Supplemental Material at http://link.aps.org/supplemental/10.1103/PhysRevB.99.165411 for layer degree of freedom for excitons in transition metal dichalcogenides.

[35] H. Wang, J. Bang, Y. Sun, L. Liang, D. West, V. Meunier, and S. Zhang, The role of collective motion in the ultrafast charge transfer in van der Waals heterostructures, Nat. Commun. **7**, 11504 (2016).

[36] G. Gupta and K. Majumdar, Fundamental exciton linewidth broadening in monolayer transition metal dichalcogenides, Phys. Rev. B **99**, 085412 (2019).

[37] M. R. Molas, K. Nogajewski, A. O. Slobodeniuk, J. Binder, M. Bartos, and M. Potemski, Optical response of monolayer, few-layer and bulk tungsten disulfide, Nanoscale **9**, 13128 (2017).

[38] A. Arora, M. Koperski, K. Nogajewski, J. Marcus, C. Faugeras, and M. Potemski, Excitonic resonances in thin films of WSe_2: From monolayer to bulk material, Nanoscale **7**, 10421 (2015).

[39] H. Zeng, G.-B. Liu, J. Dai, Y. Yan, B. Zhu, R. He, L. Xie, S. Xu, X. Chen, W. Yao et al., Optical signature of symmetry variations and spin-valley coupling in atomically thin tungsten dichalcogenides, Sci. Rep. **3**, 1608 (2013).

[40] W. Zhao, Z. Ghorannevis, L. Chu, M. Toh, C. Kloc, P.-H. Tan, and G. Eda, Evolution of electronic structure in atomically thin sheets of WS_2 and WSe_2, ACS Nano **7**, 791 (2012).

[41] G. Moody, C. Kavir Dass, K. Hao, C.-H. Chen, L.-J. Li, A. Singh, K. Tran, G. Clark, X. Xu, G. Berghäuser et al., Intrinsic homogeneous linewidthand broadening mechanisms of excitons in monolayer transition metal dichalcogenides, Nat. Commun. **6**, 8315 (2015).

[42] R. Bertoni, C. W. Nicholson, L. Waldecker, H. Hübener, C. Monney, U. De Giovannini, M. Puppin, M. Hoesch, E. Springate, R. T. Chapman et al., Generation and Evolution of Spin-, Valley-, and Layer-Polarized Excited Carriers in Inversion-Symmetric WSe_2, Phys. Rev. Lett. **117**, 277201 (2016).